APL Materials

RESEARCH ARTICLE | FEBRUARY 18 2025

Magnetoacoustic waves in a highly magnetostrictive $Fe_{72}Ga_{28}$ thin film

Marc Rovirola ; M. Waqas Khaliq ; Blai Casals ; Adrian Begué ; Neven Biskup ; Noelia Coton ; Joan Manel Hernàndez ; Miguel Angel Niño ; Michael Foerster ; Alberto Hernández-Mínguez ; Rocío Ranchal ; Marius V. Costache ; Antoni García-Santiago ; Ferran Macià ✉

APL Mater. 13, 021112 (2025)
https://doi.org/10.1063/5.0237699

Magnetoacoustic waves in a highly magnetostrictive $Fe_{72}Ga_{28}$ thin film

Cite as: APL Mater. 13, 021112 (2025); doi: 10.1063/5.0237699
Submitted: 6 September 2024 • Accepted: 17 January 2025 •
Published Online: 18 February 2025 • Corrected: 19 March 2025

Marc Rovirola,[1,2,a)] **M. Waqas Khaliq,**[3] **Blai Casals,**[2,4] **Adrian Begué,**[5,6] **Neven Biskup,**[5] **Noelia Coton,**[5] **Joan Manel Hernàndez,**[1,2] **Miguel Angel Niño,**[3] **Michael Foerster,**[3] **Alberto Hernández-Mínguez,**[7] **Rocío Ranchal,**[5,8] **Marius V. Costache,**[1,2] **Antoni García-Santiago,**[1,2] **and Ferran Macià**[1,2,b)]

AFFILIATIONS

[1] Departament de Física de la Matèria Condensada, Facultat de Física, Universitat de Barcelona, 08028 Barcelona, Spain
[2] Institut de Nanociència i Nanotecnologia (IN2UB), Universitat de Barcelona, 08028 Barcelona, Spain
[3] ALBA Synchrotron Light Source, 08290 Cerdanyola del Vallès, Spain
[4] Departament de Física Aplicada, Facultat de Física, Universitat de Barcelona, 08028 Barcelona, Spain
[5] Departamento de Física de Materiales, Facultad de Ciencias Físicas, Universidad Complutense de Madrid, 28040 Madrid, Spain
[6] Facultad de Ciencias, Universidad de Zaragoza, 50009 Zaragoza, Spain
[7] Paul-Drude-Institut für Festkörperelektronik, Leibniz-Institut im Forschungsverbund Berlin e.V., 10117 Berlin, Germany
[8] Instituto de Magnetismo Aplicado, UCM-ADIF-CSIC, Las Rozas 28232, Spain

[a)] **Electronic mail:** marc.rovirola@ub.edu
[b)] **Author to whom correspondence should be addressed:** ferran.macia@ub.edu

ABSTRACT

The interaction between surface acoustic waves and magnetization offers an efficient route for electrically controlling magnetic states. Here, we demonstrate the excitation of magnetoacoustic waves in galfenol thin films with a 28 at. % gallium composition, corresponding to the second magnetostrictive peak in bulk samples. We quantify the amplitude of the induced magnetization oscillations using magnetic imaging in an x-ray photoelectron microscope and estimate the dynamic magnetoelastic constants through micromagnetic simulations. Our findings demonstrate the potential of galfenol thin films for magnonic applications and reveal that, despite strong magnetoelastic coupling, magnetic interactions and spin-wave dispersion relations significantly influence the overall amplitude of magnetoacoustic waves.

I. INTRODUCTION

Integrating magnetic devices into electronic circuits requires efficient mechanisms for electrical control of magnetization in ferromagnetic (FM) nanomagnets, as opposed to magnetic-field control. Electric-field control of magnetism has garnered significant attention for its potential to design ultralow-power spintronic devices.[1] Current research focuses on using spin-polarized currents to exert torques on magnetic moments by transferring spin angular momentum.[2,3] Various device geometries and material combinations have been proposed to generate high spin current densities, often leveraging spin–orbit interactions through Rashba, Dresselhaus, and spin-Hall effects.[4–8] This approach allows for manipulating the magnetization in nanostructures with significantly reduced energy requirements.

Another efficient method for controlling magnetization using electric fields involves electrical tailoring of magnetic anisotropy, a high-speed technique compatible with existing technologies.[9,10] In this work, we study electrically-driven phonon coupling to magnetization[11,12] in bilayer heterostructures that combine a piezoelectric material with a highly magnetostrictive FM iron–gallium ($Fe_{72}Ga_{28}$) alloy. We use voltage-controlled surface acoustic waves

(SAWs) to generate spatially and temporally varying magnetic anisotropy in the FM alloy.

SAWs are MHz–GHz strain waves that propagate along the surface of a solid[13,14] and can originate from oscillating voltages through interdigital transducers (IDTs) in a piezoelectric material. These waves create an oscillating strain that can induce a varying magnetic anisotropy field in a magnetostrictive material.[15–17] The GHz frequency range is particularly relevant for magnetization dynamics because it matches internal resonance energies, and the associated spin waves have wavelengths in the nanometer–micrometer range.

In the past decade, numerous studies have demonstrated that SAWs can efficiently couple to magnetization via the magnetoelastic effect (ME),[18–24] focusing on the magnetoacoustic waves (MAWs) generated by SAWs.[25–30] Transition metal FMs, including Heusler alloys with similar bulk magnetostriction coefficients (~100 ppm), have shown significant variations in MAW amplitudes. Previous studies in thin films of galfenol with lower Ga content (18%–20%) have used SAWs to reduce the coercive field[31] and create magnetic patterns[32] at the microscale, demonstrating the potential for controlling magnetic states with oscillating strain. Field sensors have been proposed based on the field-dependent SAW absorption observed in thick FeGa films.[33,34]

Bulk $Fe_{100-x}Ga_x$ alloys exhibit two magnetostriction peaks: ~200 ppm for $Fe_{82}Ga_{18}$ and even higher (~400 ppm) for $Fe_{72}Ga_{28}$.[35] The first magnetostriction peak results from an increase in the magnetoelastic coupling coefficient, as the Ga content in the alloy reaches 18 at. %, while the second peak seems to arise from softening of the elastic shear constants[36,37] at about 28 at. % (i.e., a lower magnetoelasticity may result in a larger magnetostriction). In heterostructures consisting of piezoelectric substrates and magnetostrictive layers, the size of the effect depends on the coupling between the substrate and layer's strain. Softening of the shear elastic constants can thus be detrimental, as the layer becomes less rigid and may have difficulty following the strain imposed by the piezoelectric substrate at MHz–GHz speeds.

In this work, we investigate the interaction of SAWs at 500 MHz with magnetization in a 10-nm-thick $Fe_{72}Ga_{28}$ thin film, which has a rich Ga content compared with previous studies[31–34,38–40] and falls within the "second peak" of magnetostriction for FeGa alloys, a region known for enhanced magnetostrictive properties.[35,36] A thickness of 10 nm ensures that the shape anisotropy from the thin film geometry keeps the magnetization in-plane, while also keeping a low coercive field and small anisotropy.[39]

Our experiment involves placing the FM thin film on the acoustic path of a piezoelectric substrate and exciting SAWs through IDTs at 500 MHz. Due to the magnetostrictive nature of FeGa, the deformation caused by the SAWs generates an oscillating anisotropy, leading to periodic changes in the magnetization direction. We directly image the resulting MAWs using x-ray microscopy and quantify the dynamic magnetoelastic coupling.

II. EXPERIMENTAL DETAILS

The sample under study consists of a piezoelectric 127.86° Y-cut $LiNbO_3$ substrate and a 10-nm-thick FeGa film deposited by DC magnetron sputtering and patterned like a Hall bar [see Fig. 1(a)]. We deposited a 5-nm thick buffer and 2-nm thick capping molybdenum layers below and above the galfenol film to ensure good adhesion and prevent oxidation. The sample's stoichiometry is $Fe_{72}Ga_{28}$, but it will be referred to as FeGa throughout this article. More details on FeGa growth can be found elsewhere.[36] Unidirectional IDTs[41] were patterned at opposite ends of the FeGa film using electron beam lithography, metal evaporation, and lift-off [see Fig. 1(a)]. This configuration allows both the generation of SAWs that propagate along the FM film and the measurement of transmitted SAW power (S_{21} coefficient). We designed the IDTs to generate Rayleigh SAWs, characterized by in-plane and out-of-plane longitudinal strain components (ε_{xx} and ε_{zz}, respectively) and a shear

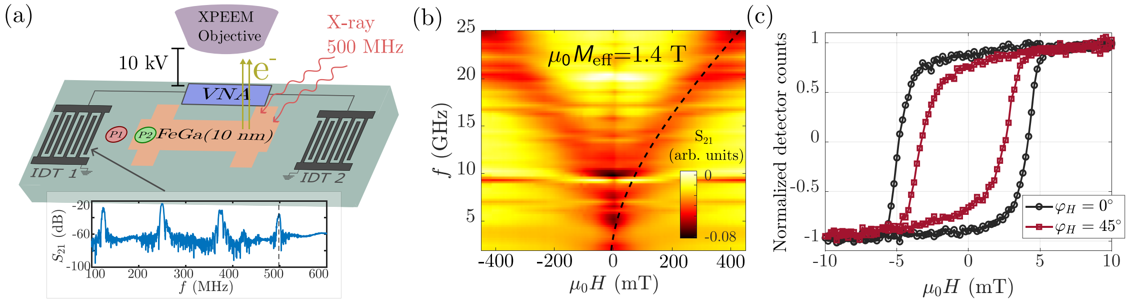

FIG. 1. (a) The top panel shows a schematic illustration of the magnetoacoustic device setup, which includes a piezoelectric substrate ($LiNbO_3$) and a magnetostrictive thin film of FeGa (10 nm). This setup also features a Mo buffer layer (5 nm) and a Mo capping layer (2 nm). The bottom panel displays the transmission coefficient (S_{21}) of the interdigital transducers (IDTs), highlighting harmonics that start at 125 MHz. The dashed vertical line marks the frequency used in the experiments (500 MHz). (b) Ferromagnetic resonance data of the FeGa film used in the magnetoacoustic device. The vertical axis represents the microwave (MW) signal frequency applied to a coplanar waveguide, inducing uniform precession in FeGa. In contrast, the horizontal axis shows the externally applied magnetic field. The color scale indicates the relative loss of MW power after the RF field excites the FeGa film, with darker shades (black and red) indicating stronger absorption of MW power by the FeGa film. The black dashed line represents the fit of Kittel's equation, from which we determine an effective magnetization saturation $\mu_0 M_{\text{eff}} = 1.4$ T. (c) Longitudinal magneto-optical Kerr effect (MOKE) hysteresis loop of the patterned FeGa for two in-plane magnetic field orientations. The black curve (circles) corresponds to a magnetic field oriented parallel to the SAWs, and the red curve (squares) corresponds to a magnetic field at 45° with respect to the SAWs. Both curves reveal a coercive field below 5 mT and full saturation around 6 mT.

strain component (ε_{xz}). The spatial periodicity of the finger-like electrodes in the IDTs was designed to excite SAWs with a fundamental frequency of 125 MHz and its corresponding harmonics [see the S_{21} spectrum in Fig. 1(a)] and to follow a linear dispersion relation $v_{\mathrm{SAW}} = f_{\mathrm{SAW}}\lambda_{\mathrm{SAW}}$ with $v_{\mathrm{SAW}} \approx 3900$ m/s. Through the magnetoelastic effect, the strain waves from the SAWs are transformed into a dynamically effective magnetic field, producing torque on the magnetization of FeGa and, thus, generating MAWs.

III. RESULTS

We initially characterized the sample using ferromagnetic resonance (FMR) and magneto-optical Kerr effect (MOKE) microscopy. We measured the FMR on a separate FeGa sample grown simultaneously with the magnetoacoustic device on an identical substrate to ensure that both objects had the same magnetic properties. In the FMR experiment, we placed the sample on a coplanar waveguide and excited it at various frequencies while sweeping the magnetic field from −400 to 400 mT. At specific magnetic fields and MW frequencies, the magnetization enters resonance, absorbing more MW power and resulting in a dip in the transmission coefficient, which appears as darker shades in Fig. 1(b). The frequency and magnetic field of these resonances follow Kittel's equation,[42]

$$f = \mu_0\gamma\sqrt{H(H + M_{\mathrm{eff}})}, \tag{1}$$

where γ is the gyromagnetic ratio ($\gamma \approx 28$ GHz/T) and $\mu_0 M_{\mathrm{eff}}$ is the effective magnetization saturation, which we estimated to be around 1.4 T. The effective magnetization saturation is given as $M_{\mathrm{eff}} = M_S - H_k$, where M_S is the magnetization saturation and H_k is the out-of-plane anisotropy field. We expect this field to be small in our FeGa films, as no metastable tetragonal phase is foreseen,[43,44] so that $M_{\mathrm{eff}} \approx M_S$. Our FeGa thin films have broad FMR peaks with a possible origin in the fluctuation in magnetic anisotropy.[45]

Figure 1(c) shows the in-plane magnetic loop of FeGa obtained through MOKE microscopy, illustrating two in-plane magnetic field orientations, $\varphi_H = 0°$ (black) and $\varphi_H = 45°$ (red). The black curve ($\varphi_H = 0°$) displays a squarer loop, characteristic of an easy axis, while the red curve ($\varphi_H = 45°$) has a hysteresis loop indicative of a hard axis. The presence of anisotropy comes from the ballistic flow regime during growth (see Ref. 46 for more information). Both loops exhibit a coercive field of less than 5 mT and full magnetic saturation at around 6 mT.

To study the effect of SAWs on the magnetization dynamics of FeGa, we used direct imaging with x-ray photoemission electron microscopy (XPEEM) at the ALBA synchrotron facility. This technique allows us to observe and quantify both SAWs and MAWs. The experiment involves illuminating the sample with x-rays at the L_3 energy edge of Fe, which excites secondary electrons. A 10 kV potential between the device and the XPEEM objective pulls out these electrons. Two types of images can be obtained: XPEEM, which is sensitive to the piezoelectric voltage at the sample surface, and x-ray magnetic circular dichroism (XMCD), which provides magnetic contrast by subtracting two images taken with opposite circular helicity, canceling non-helicity-dependent effects.

SAWs are emitted using the IDTs and propagate along the acoustic path. An AC electric field is applied to the IDT to generate SAWs at 500 MHz, synchronized with the repetition rate of the synchrotron x-ray bunches, enabling stroboscopic imaging at specific phases of the SAW.[46] The local piezoelectric field from the SAW affects the kinetic energy of the photoelectrons that are accelerated out from the piezoelectric sample and are highly sensitive to the electric field between the sample and the microscope objective. By adding a bias voltage (V_{B}) to the sample relative to the objective, we can change the contrast of the SAWs.[47] Scanning the detector counts as a function of V_{B} at opposite SAW phases allows us to measure the peak-to-peak amplitude of the piezoelectric potential at the sample surface.

The inset of Fig. 2 shows an XPEEM image of the $\mathrm{LiNbO_3}$ substrate at location P1 [see Fig. 1(a)]. The red and black rectangles represent the studied areas, corresponding to opposite SAW phases. The spectra in Fig. 2 display normalized detector counts as a function of V_{B} for each phase, with the colors matching the studied areas in the inset. Subtracting both spectra, we obtain the SAW peak-to-peak voltage (V_{pp}), the horizontal shift between both spectra. The corresponding strain amplitudes can be determined by numerically solving the coupled elastic and electromagnetic equations[48] using the values of the elastic, piezoelectric, and dielectric tensors for a 128° Y-cut $\mathrm{LiNbO_3}$ substrate[49] at a given SAW frequency and power density. In our experiment, we measured $V_{\mathrm{pp}} = 0.86$ V at 500 MHz and calculated the strain component amplitudes as $\varepsilon_{xx} = 6.4 \times 10^{-5}$, $\varepsilon_{zz} = 2.0 \times 10^{-5}$, and $\varepsilon_{xz} = 1.4 \times 10^{-5}$.

To study the MAWs excited in the FeGa film, we took a series of XMCD images at position P2 [see Fig. 1(a)] under various magnetic field strengths. First, a magnetic field over 7 mT is applied to saturate the sample. However, to eliminate any remaining static features such as magnetic domains or surface impurities at low magnetic fields, we used a four-image process: taking two images with the same x-ray helicity at a 180°-phase difference in the SAW and subtracting them, then obtaining magnetic contrast by subtracting images taken with

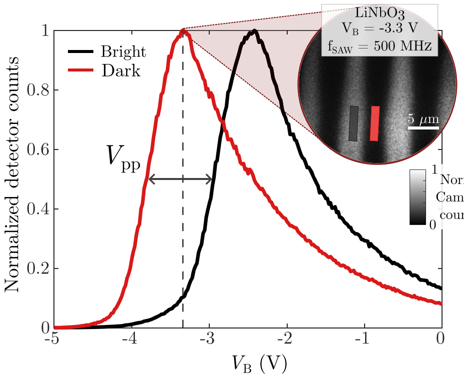

FIG. 2. Scans of bias voltage, V_{B}, for opposite SAW phases. The red line represents the dark SAW phase, while the black line represents the bright SAW phase. The horizontal displacement between the spectra is the peak-to-peak voltage of the SAW at the sample surface, $V_{\mathrm{pp}} = 0.86$ V. The inset shows an XPEEM image at location P1 on $\mathrm{LiNbO_3}$ of SAWs at 500 MHz. The black and red rectangles are the regions where we extract the curve data as we sweep the bias voltage.

opposite helicity. We call this a two-phase XMCD image. Figure 3(a) shows a standard XMCD image of magnetic domains (left) and a two-phase XMCD image of MAWs (right).

MAW can be clearly seen in two-phase XMCD images. The observed patterns shift with the synchronization and are visible only at the x-ray L_3 energy of Fe, indicating that the waves are of magnetic origin and are generated by the SAW. From the MAW images, we extracted their profile and fitted it to a sinusoidal wave, using amplitude and phase as fitting parameters [see Fig. 3(b)]. To quantify the amplitude, we normalized it by the contrast difference between opposing domains, which is proportional to the magnetization saturation (M_S). This normalized amplitude is shown in Fig. 3(c), with each black point indicating the amplitude at different magnetic fields, ranging from 1 to 6 mT. The magnetic field is applied in the film plane at a 30° angle to the SAW propagation direction to maximize the magnetoelastic torque.[19,20,50] Our MAW quantification estimates a magnetization precession angle of 1°–1.5°, with a maximum efficiency of 2.3°/strain, comparable to that of nickel[51] and Fe_3Si.[28]

Next, we compared our results to micromagnetic simulations to quantify the magnetoelastic coupling constant. The simulation consists in a partial differential equation solving of Landau–Lifshitz–Gilbert equations by generating a mask of strain that moves with the simulation running time, mimicking the SAWs. The parameters of the simulated FeGa are $\mu_0 M_s = 1.4$ T, $A_{ex} = 1.8$ pJ/m,[39] and $\alpha = 0.012$.[39] We used the MuMax3 simulation software,[53,54] which incorporates all effective field contributions, including Zeeman, demagnetization, anisotropy, and magnetoelastic fields generated by the coupling between SAWs and magnetization. The effective magnetoelastic field is given by

$$F_{\text{me}} = B_1\left[\varepsilon_{xx}m_x^2 + \varepsilon_{yy}m_y^2 + \varepsilon_{zz}m_z^2\right] + 2B_2\left[\varepsilon_{xy}m_xm_y + \varepsilon_{xz}m_xm_z + \varepsilon_{yz}m_ym_z\right], \tag{2}$$

where B_i are the magnetoelastic constants and m_i are the normalized magnetization components. Due to the in-plane magnetization and the fact that SAWs propagate in the x-direction, the ME will be primarily dominated by ε_{xx} and B_1, with B_2 having a negligible impact. Increasing B_2 from 0 to 16 MJ/m^3 results in a 2% increase in MAW amplitude at resonance. Therefore, only B_1 is determined. The SAWs are introduced in the simulation as a plane wave with amplitude ε_{ij} that moves in time. The ME effect produces an effective field that creates a torque to the magnetization, thus producing MAWs. Their amplitude is determined by calculating the wave envelope at different magnetic fields.

The results of the simulations are shown with the red solid, dotted, and dashed lines in Fig. 3(c) together with experimental data. They reveal a non-resonance broad peak at 1 mT caused by the interplay between internal effective fields (anisotropy and applied field) and the ME torque (that depends on the relative orientation of the magnetization and the SAW propagation). The simulation that better reproduces the experimental results uses $B_1 = 4.0 \pm 0.5$ MJ/m^3 and a small in-plane anisotropy of about 1 mT in the x-direction, parallel to the direction of SAW propagation. This shows that even with the reduction in the shear elastic constants from the second magnetostriction peak, we were able to generate a sizable coupling between the SAWs and the FeGa magnetization, obtaining a comparable magnetoelastic constant, B_1, as found in bulk single-crystal FeGa with similar stoichiometry ($B_1 = -4.8$ MJ/m^3).[37]

The loss of resonance at 500 MHz comes from the introduction of the wavelength parameter ($\lambda = v_s/f_{\text{SAW}}$) in the magnetic waves due to the SAWs. The non-uniform magnetization precession affects exchange and dipolar energies, typically leading to an additional increase in frequency with decreasing wavelength.[27,54] This effect is illustrated in Fig. 4(a). The black solid line corresponds to the Kittel relation [Eq. (1)] for a uniform excitation with $\lambda = \infty$ (FMR), while the red dots show resonance frequencies of the MAW with its corresponding wavelength when the SAW propagation direction and the applied magnetic field form a 30° angle (φ_H). Each point represents the MAW resonance frequency for a given magnetic field. In this case, the resonance starts around 3 GHz; thus, exciting it at 500 MHz results in non-resonant MAWs. Figure 4(b) shows the interaction

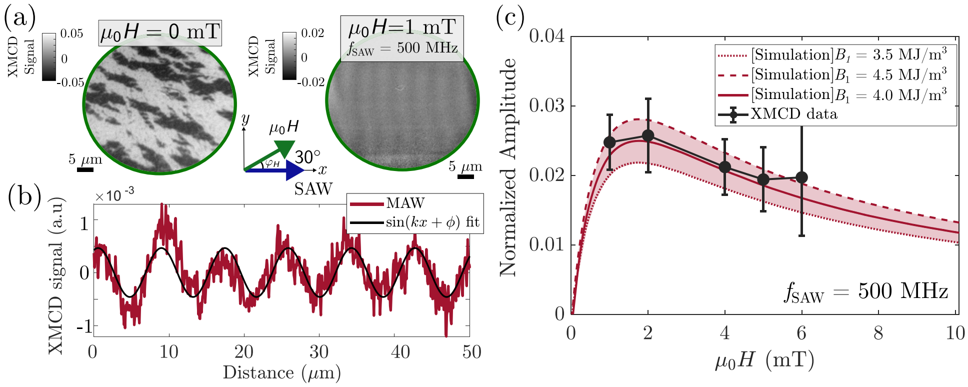

FIG. 3. (a) The left panel displays an XMCD image showing magnetic domains on FeGa. The right panel displays a 2-phase XMCD image highlighting MAWs of 500 MHz on FeGa at a magnetic field of 1 mT. (b) Spatial MAW profile (red curve) at a fixed magnetic field of 1 mT. The black curve is the fitted sinusoidal function. (c) Magnetic field dependence of the normalized MAW amplitude derived from the XMCD profiles (connected black dots; see the text for details). The red dotted, solid, and dashed lines show the resulting amplitude of micromagnetic simulations with different effective magnetoelastic constants 3.5, 4.0, and 4.5 MJ/m^3, respectively. All the simulations include a 1 mT in-plane uniaxial anisotropy in the x direction (parallel to the SAWs). The determined magnetoelastic constant that better suited the XMCD data is $B_1 = 4.0 \pm 0.5$ MJ/m^3.

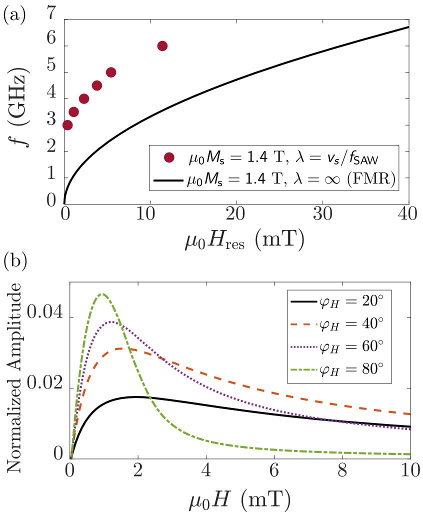

FIG. 4. (a) Resonant magnetic field for FMR (black solid line) and acoustic-FMR (red dots). The black curve (FMR) plots the Kittel relation [Eq. (1)] with $\mu_0 M_{\mathrm{eff}} = 1.4$ T. The red dots (acoustic-FMR) are the result of simulations exciting the FeGa at different SAW frequencies. (b) Results of simulations using FeGa parameters with $\mu_0 H^x_{Ku1} = 1$ mT showing the normalized amplitude of the MAWs in FeGa at different external magnetic field angles, φ_H.

between the internal effective field and the ME torque. We simulated curves of the MAW amplitude caused by the SAW at 500 MHz using the same parameters as in Fig. 3(c) but for different angles of the applied magnetic field. Increasing the applied field causes two competing effects: (i) an increase in the overall effective field, reducing the strain's influence on magnetization and (ii) a gradual tilt of magnetization from the anisotropy axis toward the magnetic field direction, which now enhances the strain's effect on magnetization. ME torque is maximum at 30° and vanishes when the magnetization moment is along the x or y axis. Thus, the magnetization at low fields is still along the anisotropy axis (x axis) with negligible torque from the SAW. As the magnetic field increases, magnetization rotates and the SAW's torque on magnetization reaches a maximum around 1–2 mT when magnetization is along the applied field. Larger magnetic fields simply cause a reduction in SAW-induced magnetization dynamics. We observe such behavior in Fig. 4(b), where all curves have a maximum around 1–2 mT with different amplitudes depending on the direction of the applied magnetic field. The saturation magnetization, M_s, plays a crucial role here as it increases resonance frequencies and lowers magnetoelastic effective fields (the effective field comes from the ratio between B_i and M_s), resulting in a smaller MAW response.

IV. CONCLUSIONS

To summarize, we investigated the dynamic interaction between SAWs and magnetization in a galfenol thin film with 28 at. % in gallium content on a piezoelectric $LiNbO_3$ substrate. We demonstrated the electric control of magnetization waves through XPEEM measurements. Our findings revealed the presence of both SAWs and magnetoacoustic waves (MAWs) in the FM thin film, with the MAW amplitude being comparable to that in cobalt but smaller than in nickel. Our technique allows quantification of strain and MAW amplitude and, thus, enables us to obtain an estimate for the magnetoelastic constant ($B_1 = 4.0 \pm 0.5$ MJ/m^3) in the sputtered 10 nm galfenol thin film with a rich Ga content ($Fe_{72}Ga_{28}$). Our simulations indicate that we generate MAWs in a non-resonance mode and suggest that we can obtain larger MAW amplitudes when resonance conditions are fulfilled. The simulations also show that the propagation angle between the MAW and magnetization plays a crucial role in determining the resonance condition and setting the overall MAW amplitude.

ACKNOWLEDGMENTS

The experiments were performed at the CIRCE beamline at the ALBA Synchrotron with the collaboration of ALBA staff. M.R., M.W.K., B.C., M.V.C., A.G.S., J.M.H., and F.M. acknowledge funding from Grant No. MCIN/AEI/10.13039/501100011033 through Grant No. PID2020-113024I00, PID2022-136762NA-I00, PID2023-150721OB-I00 and EU NextGenerationEU/PRTR through Grant No. PDC-2023-145910-I00. MR was supported by FPI Grant No. PRE2021-097235. A.B., N.C., M.F., M.A.N. and R.R. acknowledge Project No. PID2021-122980OB-C51 and PID2021-122980OB-C54 (AEI/FEDER) of the Spanish Ministry of Science and Innovation. A.B. would like to acknowledge the funding received from the Ministry of Universities and the European Union-Next Generation for the Margarita Salas fellowship. MWK aknowledges CAEM project (funded by the Ministry of Science and Innovation and the Generalitat de Catalunya, with the support of NextGeneration EU funds).

AUTHOR DECLARATIONS

Conflict of Interest

The authors have no conflicts to disclose.

Author Contributions

Marc Rovirola: Conceptualization (equal); Data curation (lead); Formal analysis (lead); Methodology (lead); Writing – original draft (lead); Writing – review & editing (lead). **M. Waqas Khaliq**: Data curation (equal); Methodology (equal); Writing – review & editing (supporting). **Blai Casals**: Data curation (equal); Funding acquisition (equal); Methodology (equal); Writing – review & editing (supporting). **Adrian Begué**: Data curation (supporting); Resources (supporting). **Neven Biskup**: Data curation (supporting); Methodology (supporting); Writing – review & editing (supporting). **Noelia Coton**: Data curation (supporting); Writing – review & editing (supporting). **Joan Manel Hernàndez**: Conceptualization (equal); Data curation (equal); Formal analysis (equal); Funding acquisition (equal); Investigation (equal); Methodology (lead); Project administration (equal); Supervision (equal); Writing – review & editing (equal). **Miguel Angel Niño**: Data curation (supporting); Methodology (equal); Writing – review & editing (supporting). **Michael Foerster**: Conceptualization (lead); Data curation (equal); Funding acquisition (lead); Methodology (lead); Project administration (equal); Writing – review & editing (equal). **Alberto Hernández-Mínguez**: Resources (equal); Writing – original

draft (equal); Writing – review & editing (equal). **Rocío Ranchal**: Conceptualization (lead); Data curation (equal); Funding acquisition (lead); Resources (equal); Writing – review & editing (equal). **Marius V. Costache**: Data curation (equal); Writing – original draft (equal); Writing – review & editing (equal). **Antoni García-Santiago**: Data curation (equal); Writing – original draft (equal); Writing – review & editing (equal). **Ferran Macià**: Conceptualization (lead); Data curation (equal); Formal analysis (equal); Funding acquisition (lead); Project administration (lead); Supervision (lead); Validation (lead); Writing – original draft (lead); Writing – review & editing (lead).

DATA AVAILABILITY

The data that support the findings of this study are available from the corresponding author upon reasonable request.

REFERENCES

[1] F. Matsukura, Y. Tokura, and H. Ohno, Nat. Nanotechnol. **10**, 209 (2015).
[2] J. Slonczewski, J. Magn. Magn. Mater. **159**, L1 (1996).
[3] L. Berger, Phys. Rev. B **54**, 9353 (1996).
[4] G. Dresselhaus, Phys. Rev. **100**, 580 (1955).
[5] A. Chernyshov *et al.*, Nat. Phys. **5**, 656 (2009).
[6] I. Mihai Miron *et al.*, Nat. Mater. **9**, 230 (2010).
[7] L. Liu *et al.*, Science **336**, 555 (2012).
[8] L. Wang *et al.*, Phys. Rev. Lett. **116**, 196602 (2016).
[9] D. Chiba *et al.*, Nature **455**, 515 (2008).
[10] V. Iurchuk, J. Bran, M. Acosta, and B. Kundys, Appl. Phys. Lett. **122**, 072404 (2023).
[11] A. A. Bukharaev, A. K. Zvezdin, A. P. Pyatakov, and Y. K. Fetisov, Phys.-Usp. **61**, 1175 (2018).
[12] M. Foerster and F. Macià, J. Phys. Condens. Matter **31**, 190301 (2019).
[13] A. K. Ganguly, K. L. Davis, D. C. Webb, and C. Vittoria, J. Appl. Phys. **47**, 2696 (1976).
[14] I.-a. Feng, M. Tachiki, C. Krischer, and M. Levy, J. Appl. Phys. **53**, 177 (1982).
[15] W.-G. Yang and H. Schmidt, Appl. Phys. Rev. **8**, 021304 (2021).
[16] J. Puebla, Y. Hwang, S. Maekawa, and Y. Otani, Appl. Phys. Lett. **120**, 220502 (2022).
[17] P. Delsing *et al.*, J. Phys. D: Appl. Phys. **52**, 353001 (2019).
[18] J. M. Hernandez, P. V. Santos, F. Macià, A. García-Santiago, and J. Tejada, Appl. Phys. Lett. **88**, 012503 (2006).
[19] M. Weiler *et al.*, Phys. Rev. Lett. **106**, 117601 (2011).
[20] L. Dreher *et al.*, Phys. Rev. B **86**, 134415 (2012).
[21] M. Weiler *et al.*, Phys. Rev. Lett. **108**, 176601 (2012).
[22] P. G. Gowtham, T. Moriyama, D. C. Ralph, and R. A. Buhrman, J. Appl. Phys. **118**, 233910 (2015).
[23] D. Labanowski, A. Jung, and S. Salahuddin, Appl. Phys. Lett. **108**, 022905 (2016).
[24] K. M. Seemann *et al.*, Phys. Rev. B **105**, 144432 (2022).
[25] P. Kuszewski *et al.*, J. Phys.: Condens. Matter **30**, 244003 (2018).
[26] C. Müller *et al.*, Adv. Electron. Mater. **8**, 2200033 (2022).
[27] B. Casals *et al.*, Phys. Rev. Lett. **124**, 137202 (2020).
[28] M. Rovirola *et al.*, Phys. Rev. Appl. **20**, 034052 (2023).
[29] M. W. Khaliq *et al.*, Phys. Rev. Mater. **8**, 084406 (2024).
[30] M. Rovirola *et al.*, Phys. Rev. Res. **6**, 023285 (2024).
[31] W. Li, B. Buford, A. Jander, and P. Dhagat, IEEE Trans. Magn. **50**, 37 (2014).
[32] W. Li, B. Buford, A. Jander, and P. Dhagat, J. Appl. Phys. **115**, 17E307 (2014).
[33] W. Li, P. Dhagat, and A. Jander, IEEE Trans. Magn. **48**, 4100 (2012).
[34] Y. Sun *et al.*, Appl. Sci. **11**, 11726 (2021).
[35] Q. Xing, Y. Du, R. McQueeney, and T. Lograsso, Acta Mater. **56**, 4536 (2008).
[36] P. Bartolomé, A. Begué, A. Muñoz-Noval, M. Ciria, and R. Ranchal, J. Phys. Chem. C **124**, 4717 (2020).
[37] A. E. Clark *et al.*, J. Appl. Phys. **93**, 8621 (2003).
[38] M. P. Ruffoni *et al.*, Phys. Rev. Lett. **101**, 147202 (2008).
[39] D. B. Gopman, V. Sampath, H. Ahmad, S. Bandyopadhyay, and J. Atulasimha, IEEE Trans. Magn. **53**, 1 (2017).
[40] J.-Y. Duquesne, C. Hepburn, P. Rovillain, and M. Marangolo, J. Phys.: Condens. Matter **30**, 394002 (2018).
[41] Our design consists of four electrodes per period: A ground electrode, two signal electrodes of different widths, and a floating electrode between the two signal electrodes. This design provides both unidirectionality and excitation of even and odd harmonics. The total number of electrode periods in each IDT is 20.
[42] C. Kittel, Phys. Rev. **73**, 155 (1948).
[43] M. Barturen *et al.*, Phys. Rev. B **92**, 054418 (2015).
[44] P. Bartolomé, M. Maicas, and R. Ranchal, J. Magn. Magn. Mater. **514**, 167183 (2020).
[45] A. Begué, M. G. Proietti, J. I. Arnaudas, and M. Ciria, J. Magn. Magn. Mater. **498**, 166135 (2020).
[46] A. Muñoz-Noval, A. Ordóñez-Fontes, and R. Ranchal, Phys. Rev. B **93**, 214408 (2016).
[47] M. Foerster *et al.*, Nat. Commun. **8**, 407 (2017).
[48] M. Foerster *et al.*, J. Synchrotron Radiat. **26**, 184 (2019).
[49] B. A. Auld, *Acoustic Fields and Waves in Solids* (Krieger Publishing Company, 1990).
[50] Lithium niobate properties, https://www.roditi.com/SingleCrystal/LiNbO3/liNBO3-Properties.html.
[51] J. Puebla *et al.*, J. Phys. D: Appl. Phys. **53**, 264002 (2020).
[52] F. Vanderveken *et al.*, Open Res. Eur. **1**, 35 (2021).
[53] A. Vansteenkiste *et al.*, AIP Adv. **4**, 107133 (2014).
[54] B. A. Kalinikos and A. N. Slavin, J. Phys. C: Solid State Phys. **19**, 7013 (1986).